endocytosis, as would be expected of a receptor in coated pits, is unknown. How much of the GP330 molecule is shed in the form of immune complexes is also unknown. The eventual availability of a full-length cDNA should allow a detailed analysis of how much of this protein is shed rather than endocytosed and why. An analysis of the antigenic sites recognized by the pathogenic autoantibodies by use of nested sets of synthetic peptides (*21*) and a determination of their location in this membrane glycoprotein may reveal the autoimmune basis of Heymann nephritis and its human counterpart.

REFERENCES AND NOTES

1. D. Kerjaschki and M. G. Farquhar, *Proc. Natl. Acad. Sci. U.S.A.* **79**, 5557 (1982).
2. W. Heymann, D. B. Hackle, S. Harwood, J. L. P. Hunter, *Proc. Soc. Exp. Biol. Med.* **100**, 660 (1959); D. Kerjaschki and M. G. Farquhar, *J. Exp. Med.* **157**, 667 (1983).
3. S. Doxsey, D. Kerjaschki, M. G. Farquhar, *J. Cell Biol.* **97**, 178a (1983); F. Chatelet *et al.*, *Am. J. Pathol.* **122**, 512 (1986).
4. D. Kerjaschki *et al.*, *Am. J. Pathol.* **129**, 183 (1987).
5. J. L. Niles *et al.*, *Kidney Int.* **31**, 338 (1987).
6. T. Yamamoto *et al.*, *Cell* **39**, 27 (1984); J. L. Goldstein *et al.*, *Annu. Rev. Cell Biol.* **1**, 1 (1985).
7. A. Ullrich *et al.*, *Nature* **309**, 418 (1984); A. McClelland, L. C. Kuhn, F. H. Ruddle, *Cell* **39**, 267 (1984); C. Schneider, M. J. Owen, D. Banville, J. G. Williams, *Nature* **311**, 675 (1984); K. Drickamer, J. F. Mamon, G. Binns, J. O. Leung, *J. Biol. Chem.* **259**, 770 (1984); K. E. Mostov, M. Friedlander, G. Blobel, *Nature* **308**, 37 (1984).
8. J. J. Kanalas and S. P. Makker, *J. Immunol.* **141**, 4152 (1988).
9. J. Gutmann *et al.*, *Am. J. Physiol.* in press.
10. W. W. Wong, L. B. Klickstein, J. A. Smith, J. H. Weis, D. T. Fearon, *Proc. Natl. Acad. Sci. U.S.A.* **82**, 7711 (1985).
11. T. V. Huynh, R. A. Young, R. W. Davis, in *DNA Cloning: A Practical Approach*, D. M. Glover, Ed. (IRL Press, Oxford, 1985), vol. 1, pp. 49–78.
12. F. Sanger and A. R. Coulson, *J. Mol. Biol.* **94**, 441 (1975).
13. D. J. Lipman and W. R. Pearson, *Science* **227**, 1435 (1985).
14. A. Gray, T. J. Dull, A. Ullrich, *Nature* **303**, 722 (1983); J. Scott *et al.*, *Science* **221**, 236 (1983).
15. J. Devereux, P. Haeberli, O. Smithies, *Nucleic Acids Res.* **12**, 387 (1984).
16. A. G. Rao *et al.*, *Biochemistry* **26**, 3556 (1987); O. M. Z. Howard, A. G. Rao, J. M. Sodez, *ibid.*, p. 3565; K. K. Stanley *et al.*, *EMBO J.* **4**, 375 (1985).
17. J. Herz *et al.*, *EMBO J.* **7**, 4119 (1988).
18. D. M. Bai *et al.*, *J. Biol. Chem.* **261**, 12395 (1986).
19. K. Kamata, L. G. Baird, M. E. Erikson, A. B. Collins, R. T. McCluskey, *J. Immunol.* **135**, 2400 (1985).
20. G. Camussi *et al.*, *ibid.*, p. 2409.
21. R. A. Houghten, *Proc. Natl. Acad. Sci. U.S.A.* **82**, 5231 (1985).

22. This work was supported by a grant from Hoechst Aktiengesellschaft (Frankfurt/Main, West Germany) and NIH grants P01-DK38452 and R01-DK18729. The authors acknowledge L.-W. Lin and L. B. Klickstein for technical discussions. We also thank M. Foucre, P. Gallant, and G. Hannigan for technical assistance.

6 January 1989; accepted 21 April 1989

Neptune Cloud Structure at Visible Wavelengths

H. B. HAMMEL

Digital images of Neptune showing cloud structure at visible wavelengths were obtained in July 1988. A discrete bright feature was detected both at 6190 Å (a weak methane absorption band in the visible) and at 8900 Å (a stronger methane band in the near infrared). The images also revealed that Neptune's southern pole was bright relative to planetary mid-latitudes at 6190 Å but not 8900 Å. The implications of these findings for atmospheric rotation and structure are discussed. The detection of discrete features at visible wavelengths is of special importance to the upcoming Voyager encounter with Neptune: the wide-angle camera has a 6190 Å filter similar to that used for these observations.

FOR THE PAST DECADE, THE PLANET Neptune has shown a remarkable amount of variability on time scales ranging from hours to years (*1*). In 1987, the diurnal variation of Neptune's disk-integrated flux was caused by a single atmospheric inhomogeneity (discrete feature), with the observed fluctuations attributable to the appearance and disappearance of this feature during planetary rotation (*2*). Many earlier images of the planet show discrete cloud features on Neptune, but these images were always obtained at 8900 Å, a strong near-infrared methane absorption band where the contrast between features and the surrounding atmosphere is enhanced (*3–5*). No images at visible wavelengths have shown discrete features (*5*), even though their presence at these wavelengths was inferred from disk-integrated photometry that showed strong diurnal variation (*6, 7*). In this paper I present new images obtained at visible wavelengths that show discrete cloud features.

The new images of Neptune (shown in Fig. 1) are a subset of data obtained with the University of Hawaii 2.24-m telescope (Mauna Kea Observatory, Hawaii) on 11 to 15 July 1988 through filters centered on three methane bands (6190, 7270, and 8900 Å) and three nearby continuum regions (6340, 7490, and 8260 Å). Each pixel of the 576 by 385 charge-coupled device (CCD) array corresponded to 0.202 arc sec on the sky. The disk of Neptune subtended approximately 2.3 arc sec; the size of the seeing disk was about 0.5 arc sec. The images were reduced by subtracting a constant bias level (typically on the order of 5340 data numbers), and then dividing by a flat-field frame. I obtained flat-field frames by exposing the CCD to the illuminated inner surface of the telescope dome through each filter each night. The final flat field for each night at each wavelength was the average of all flats obtained at that wavelength that night, normalized to unity.

Figure 1 shows a time sequence of Neptune images at two methane band wavelengths. At both wavelengths, a discrete bright feature can be seen moving from left to right as the planet rotates. The images on the left (at 6190 Å) show discrete cloud structure; all earlier images showing discrete features were obtained at 8900 Å (shown in the right-hand column). Each image in Fig. 1 is expanded from the original by a factor of 4 by means of a sinc interpolation function. In practice, this technique smooths across pixel boundaries. Only large-scale features are true features associated with Neptune (see Fig. 1); "features" that are smaller than a tenth of a planetary diameter are not true features on the planet, but pixel-to-pixel variations in the detector.

From the feature's apparent motion as the planet rotates, an atmospheric rotation period can be derived. In the past, a number of different rotation periods were deduced from the variability of Neptune, ranging from 17.0 ± 0.05 up to 18.4 ± 0.01 hours (*4*). Because the diverse measurements of Neptune's period came from observations at a variety of wavelengths ranging from the visible (6190 Å) out to the near infrared (at 1.25 and 2.2 μm), the discrepancy of periods was attributed to wavelength, that is, different wavelengths were probing to different depths in the atmosphere (*6, 8, 9*). In 1988, the dominant atmospheric rotation period was 17.7 ± 0.5 hours, based on observations of transits of the brightest feature in several series of 8900 Å images (*10*) and on disk-integrated photometry of the planet at 8900 Å (*11*). But the 17.0-hour period found in 1986 and 1987 was also determined at 8900 Å (*2*). Furthermore, measurements of the feature's location on the disk of the planet indicate that in 1988 the same feature was detected at both 6190 and 8900 Å (Fig. 1). Thus the period at 6190 Å is the same as that found from 8900

Jet Propulsion Laboratory, Pasadena, CA 91109.

Å data: 17.7 ± 0.5 hours, significantly different from the 18.4-hour period seen at this same wavelength in 1977 (*6*). The observed difference in period is evidently not due to wavelength of the observation.

An alternative explanation for the difference is latitudinal variation, that is, zonal wind systems (*6, 8, 12*). The direct observations of discrete features over the last few years support this explanation. In 1986 and 1987, the brightest cloud feature was located at −38° ± 3° and had an atmospheric rotation period of 17.00 ± 0.05 hours (*2*). But the latitude of the brightest feature in 1988 was −30° ± 2°, with an atmospheric rotation period of 17.7 ± 0.5 hours (*11*). This corresponds to a difference in zonal winds on the order of 170 m/s, comparable to that seen on the other major planets (*13*).

The images also reveal that Neptune's southern pole appeared bright relative to planetary midlatitudes at 6190 Å but not 8900 Å (see the top two images in Fig. 1). The polar brightening is visible only when the discrete bright feature is close to the edge of the planetary disk or on the hemisphere opposite Earth (that is, not visible from Earth). The discrete feature is so much brighter than the rest of the planet that when it is on the visible disk, features with smaller contrast (like the polar brightening) are no longer discernible. However, no detectable polar brightening is seen in the earliest 8900 Å image, even though the discrete bright feature is barely visible on the edge of the planet's disk. This implies that at 8900 Å the polar brightening is of extremely low contrast, if present at all.

Because of this wavelength dependence, the altitude of the scattering material that produces the polar brightening can be estimated. At these wavelengths, methane molecules in Neptune's atmosphere are very absorbing, causing the planet to appear very dark. But scattering material located fairly high in the atmosphere reflects sunlight before it penetrates deep enough to be absorbed, causing the regions with this material to appear brighter than the rest of the planet. Furthermore, the methane molar fraction above the tropopause on Neptune is thought to be unusually large. Normally, one would expect that methane would condense out of Neptune's atmosphere at the temperature minimum (located at a depth corresponding to 0.2 to 0.3 bar); if so, the methane molar fraction above this level would be quite small, on the order of 1×10^{-5}, as is seen on Uranus (*14*). However, observations of Neptune's infrared spectra and models of its thermal structure indicate that its methane molar fraction may be 0.02 or greater (*14, 15*). Therefore, the contrast at methane band wavelengths between high-altitude inhomogeneities and the surrounding atmosphere should be especially strong; the contrast at 8900 Å (a strong absorption band) is expected to be greater than that at 6190 Å (a weaker band).

Recent studies of the vertical aerosol distribution of Neptune indicate that a significant brightening at the weak methane band (6190 Å) without a corresponding brightening at the strong band (8900 Å) implies that the material causing the brightening would probably be located at or below 50 mbar, for methane molar fraction of 0.025 (*16*). For comparison, photochemical models indicate that hydrocarbon hazes (formed of ethane, acetylene, and diacetylene condensates) are probably located in the region above 15 mbar (*17*). The observed limb-brightening in methane band images does indicate the presence of an aerosol layer at this higher pressure level (*16*). The polar brightening is thus probably caused by a different aerosol layer, perhaps a methane condensate cloud, at slightly greater depths.

The visible wavelength images reported here are of special importance to the Voyager 2 encounter with Neptune (scheduled for 24 August 1989). The wide-angle camera on the Voyager 2 spacecraft has a methane band filter similar to the filter used for these observations (*18*). Therefore, when Voyager 2 is close enough to Neptune (sometime after April 1989), its methane band images should show distinct cloud features and a polar haze. Voyager's excellent spatial resolution during the encounter (an increase of a factor of 1000 over ground-based resolution) will complement Earth-based observations which have greater spectral coverage (imaging longward of 7000 Å) and a longer time base (more than 10 years). Ground-based observations are being planned to coordinate with the Voyager imaging sequences.

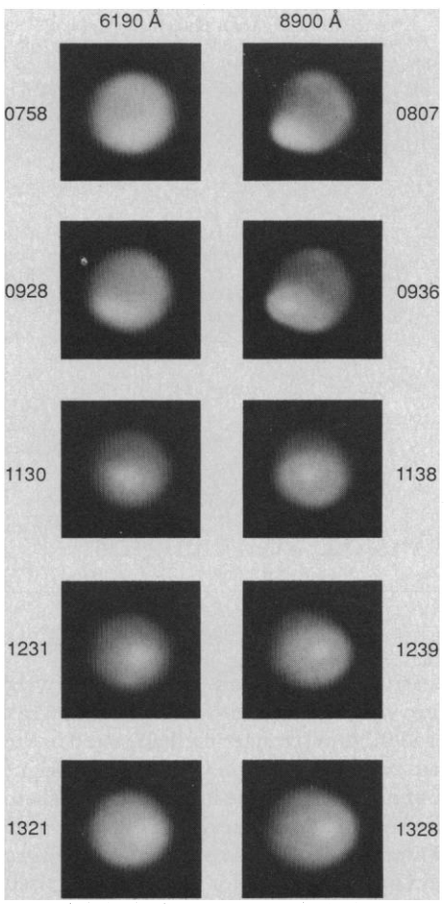

Fig. 1. The figure shows a series of images of Neptune taken at two different wavelengths on 14 July 1988 [starting times of each exposure (in universal time) are shown in the figure margins]. The time sequence advances from top to bottom in each column. Not only do these new images show discrete clouds at mid-latitudes at near-infrared wavelengths (8900 Å, right column), they are the first images to show a feature at visible wavelengths (6190 Å, left column) and revealed the presence of a haze layer covering the southern polar region on Neptune (top left image). The discrete feature can be seen moving across the disk as the planet rotates. The Voyager 2 spacecraft's wide-angle camera has a filter similar to the 6190 Å filter used to obtain the images in the left. North is up and east is to the left (Neptune's rotation axis is about 14° from north toward east, tilted about 27° back from the plane of the sky so that the southern pole is visible).

REFERENCES AND NOTES

1. For a review, see D. P. Cruikshank, *Icarus* **64**, 107 (1985).
2. H. B. Hammel, N. L. Lark, M. A. Rigler, T. J. Kreidl, *ibid.*, in press.
3. B. A. Smith, H. J. Reitsema, S. M. Larson, *Bull. Am. Astron. Soc.* **11**, 570 (1979); R. J. Terrile and B. A. Smith, *ibid.***15**, 858 (1983); J. N. Heasley, *Publ. Astron. Soc. Pacific* **96**, 767 (1984); J. N. Heasley, C. B. Pilcher, R. R. Howell, J. J. Caldwell, *Icarus* **57**, 432 (1984); B. A. Smith, in *Uranus and Neptune, Conference Publication 2330*, J. T. Bergstralh, Ed. (NASA, Washington, DC, 1984), pp. 213–223; M. J. S. Belton and R. Terrile, *ibid.*, pp. 327–347; H. B. Hammel, *Icarus*, in press.
4. H. B. Hammel and M. W. Buie, *Icarus* **72**, 62 (1987).
5. H. B. Hammel, thesis, University of Hawaii at Manoa (1988).
6. D. Slavsky and H. J. Smith, *Astrophys. J.* **226**, L49 (1978).
7. H. J. Smith and D. Slavsky, *Bull. Am. Astron. Soc.* **12**, 704 (1980).
8. M. J. S. Belton, L. Wallace, S. Howard, *Icarus* **46**, 263 (1981).
9. R. H. Brown, D. P. Cruikshank, A. T. Tokunaga, *ibid.* **47**, 159 (1981).
10. H. B. Hammel, *Bull. Am. Astron. Soc.* **20**, 824 (1988).
11. ——— and J. Harrington, in preparation.
12. G. S. Golitsyn, *Icarus* **38**, 333 (1979).
13. A. P. Ingersoll, R. F. Beebe, B. J. Conrath, G. E. Hunt, in *Saturn*, T. Gehrels and M. S. Matthews, Eds. (Univ. of Arizona Press, Tucson, 1984), pp. 195–238.
14. G. S. Orton *et al.*, *Icarus* **70**, 1 (1987).
15. J. F. Appleby, *ibid.* **65**, 383 (1986).
16. H. B. Hammel, K. H. Baines, J. T. Bergstralh, *ibid.*, in press.
17. P. N. Romani and S. K. Atreya, *ibid.* **74**, 424 (1988).
18. The Voyager 2 spacecraft's methane filter is centered at 6184 Å, with a full width at half maximum of 60 Å [B. A. Smith *et al.*, *Space Sci. Rev.* **21**, 103 (1977)]. The filter used for these visible-wavelength

observations is centered at 6190 Å, with a 30 Å full width at half maximum (5).
19. I thank C. B. Pilcher, D. P. Cruikshank, and J. L. Elliot for many helpful discussions. Support for the observations at Mauna Kea Observatory came, in part, from the Voyager Mission. CCD research at the Institute for Astronomy (Honolulu, HI) is partially supported by NSF grants AST-8615631 and AST-8514575. This work was done while I held a National Research Council Resident Research Associateship at the Jet Propulsion Laboratory, California Institute of Technology, which is under a contract with the National Aeronautics and Space Administration.

20 March 1989; accepted 20 April 1989

Expression of a Bacterial Gene in a Trypanosomatid Protozoan

VIVIAN BELLOFATTO AND GEORGE A. M. CROSS

A simple and reproducible assay for DNA-mediated transfection in the trypanosomatid protozoan *Leptomonas seymouri* has been developed. The assay is based on expression of the *Escherichia coli* chloramphenicol acetyl transferase (CAT) gene flanked by *Leptomonas* DNA fragments that are likely to contain necessary elements for gene expression in trypanosomes. After electroporation of cells in the presence of plasmid DNA, CAT activity was detected in crude cell lysates. No activity was detected when the orientation of the *L. seymouri* mini-exon sequence (placed upstream of the CAT gene) was reversed, or in additional control experiments. This system provides a method for defining transcriptional control elements in trypanosomes.

MOLECULAR STUDIES HAVE REvealed many distinctive features of gene expression in the trypanosomatid protozoa. Mature mRNAs result from the joining of two exons, which are initially transcribed as separate RNAs. In *Trypanosoma brucei*, the 5′ exon common to all characterized mRNAs is transcribed as a short nonpolyadenylated RNA, the mini-exon donor RNA (medRNA), whose 5′ 39 nucleotides (nt) (the mini-exon) are spliced, in trans, onto an independently transcribed coding exon during mRNA maturation (*1, 2*). Trans-splicing is probably necessary to process polycistronic RNAs, whose existence in trypanosomes has been demonstrated (*3*) or implied (*4, 5*).

The medRNA genes of different trypanosomatids are mostly arranged in tandem arrays, and share sequence motifs within the mini-exon, at the medRNA exon-intron junction and at the presumed site of transcription termination (*6–8*). The identification of a complex methylated cap structure on the 5′ end of medRNA isolated from *T. brucei* indicates that medRNA transcription initiates at the conserved 5′ AACTAA sequence of medRNA (*9*), which is consistent with the results of transcription studies in isolated nuclei (*2*). Thus, it is likely that RNA polymerase promoter recognition sites are present within each reiterated unit, upstream of the 5′ end of medRNA. However, in the absence of an experimental genetic or in vitro system, it has been impossible to define the genetic elements that are essential for transcription initiation and for RNA maturation and stability.

We are developing *Leptomonas seymouri*, an insect trypanosomatid, as a model system for studying RNA transcription and splicing because large quantities can be grown axenically and individual cells can form colonies on agar plates (*4, 6*). Three laboratories have published their experiences in the pursuit of DNA-mediated transfection of trypanosomes. All of these studies relied on the detection of nucleic acid in potentially transfected cells, and were either unconvincing (*10*) or unrepeatable (*11*). To detect transfection, we utilized a plasmid (pAL5) incorporating the *Escherichia coli* chloramphenicol acetyltransferase (CAT) gene. Trypanosomes have no intrinsic CAT activity (Table 1). By measuring enzyme activity and not relying on the detection of nucleic acid as a measure of DNA uptake and expression, we were able to use large amounts of DNA without the danger of false positive results caused by DNA contamination of RNA preparations.

We surrounded the CAT coding region with *L. seymouri* sequences that we judged likely to contain control signals on the basis of available information concerning transcription of these sequences (*1, 4, 6, 7*). As all translated mRNAs in trypanosomes possess the mini-exon sequence at their 5′ end (*12*), we placed the *L. seymouri* mini-exon sequence and 304 nt of upstream sequence 5′ to the CAT coding region. To avoid the processing and potential loss of the mini-exon, which we intended to be fused directly to the 5′ end of CAT mRNA (rather than added by trans-splicing), we constructed pAL5 such that the dinucleotide sequence GT, normally found at the 5′ intron end of medRNA (*1, 6, 7, 8*), was absent from the region between the mini-exon sequence and the CAT coding sequence. To provide polyadenylation signals to the pAL5-derived mRNA, we placed the 3′ end and down-

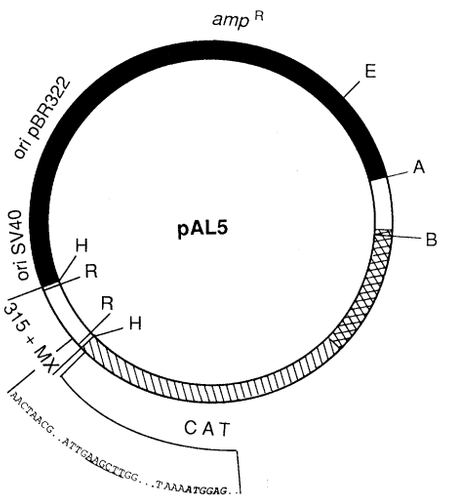

Fig. 1. Construction of plasmid pAL5 (5.9 kb). Plasmid pAL1 was constructed as follows: the 4.6-kb Apa I–Hpa I fragment from pSV2CAT (*14*) was ligated to a 700-bp Ava II–Hind III fragment from pST3 (*4*) (Ava II site filled in; Hind III site is present within the pUC12 polylinker region of pST3) and to the 290-bp Hind III–Apa I fragment from pM4 (*6*) in a single reaction. Consequently, pAL1 has, counterclockwise from the Apa I site: an ampicillin resistance gene, the pBR322 ori and the SV40 ori (black box); the CAT gene, small-t intron, and part of the SV40 early region lacking the polyadenylation signals (hatched box); the *L. seymouri* α-tubulin gene 3′ end and downstream region (cross-hatched box) and the *L. seymouri* mini-exon gene 3′ end and surrounding region (open box). pAL2, which contains a single Hind III site 36 bp upstream of the CAT gene, was constructed by deleting a Hind III site in pAL1 that is between the α-tubulin and 3′ medRNA regions. To generate pAL5, the 334-bp Rsa I fragment of pM4, which contains 304 bp of upstream sequence and the 5′ 30 bp of the mini-exon, was cloned into the Hind III site of pAL2 after ligation to an adaptor

5′ ACTTTATTGA
TGAAATAACTTCGA

that completes the mini-exon and provides Hind III ends. In pAL3, the orientation of this fragment (315 + MX; open box) is reversed. The sequence of the mini-exon–CAT region was confirmed by DNA sequencing. The three portions of sequence shown are, from left to right: the mini-exon 5′ end; the mini-exon 3′ end and Hind III site (underlined), generated by adaptor addition; and the translational start (boldface type) of the CAT gene. The two Hind III (H) and Rsa I (R) sites, the Apa I (A) site used in the construction of pAL1, the unique Bam HI (B) and Eco RI (E) sites, and the positions of the pBR322 ori, the SV40 ori, and the ampicillin resistance gene (*amp*) gene, are indicated.

Laboratory of Molecular Parasitology, The Rockefeller University, New York, NY 10021.